Nano Research

ISSN 1998-0124 CN 11-5974/O4
https://doi.org/10.26599/NR.2026.94908811

Research Article

Pulsed pumping on piezoelectric PVDF alignment layer suppresses emission consumption of DCM within cholesteric liquid crystal-host

Yang Liu(✉), Chunyang Dai, Xiaohui Gong, Hao Liu, Yongfang Zhang, Jianhua Shang(✉)
School of Information and Intelligent Science, Donghua University, 2999 North Renmin Road, Songjiang District, Shanghai 201620, China

Nano Res., **Just Accepted Manuscript** • https://doi.org/10.26599/NR.2026.94908811
https://www.sciopen.com/journal/1998-0124 on May. 6, 2026

Just Accepted

TABLE OF CONTENTS (TOC)

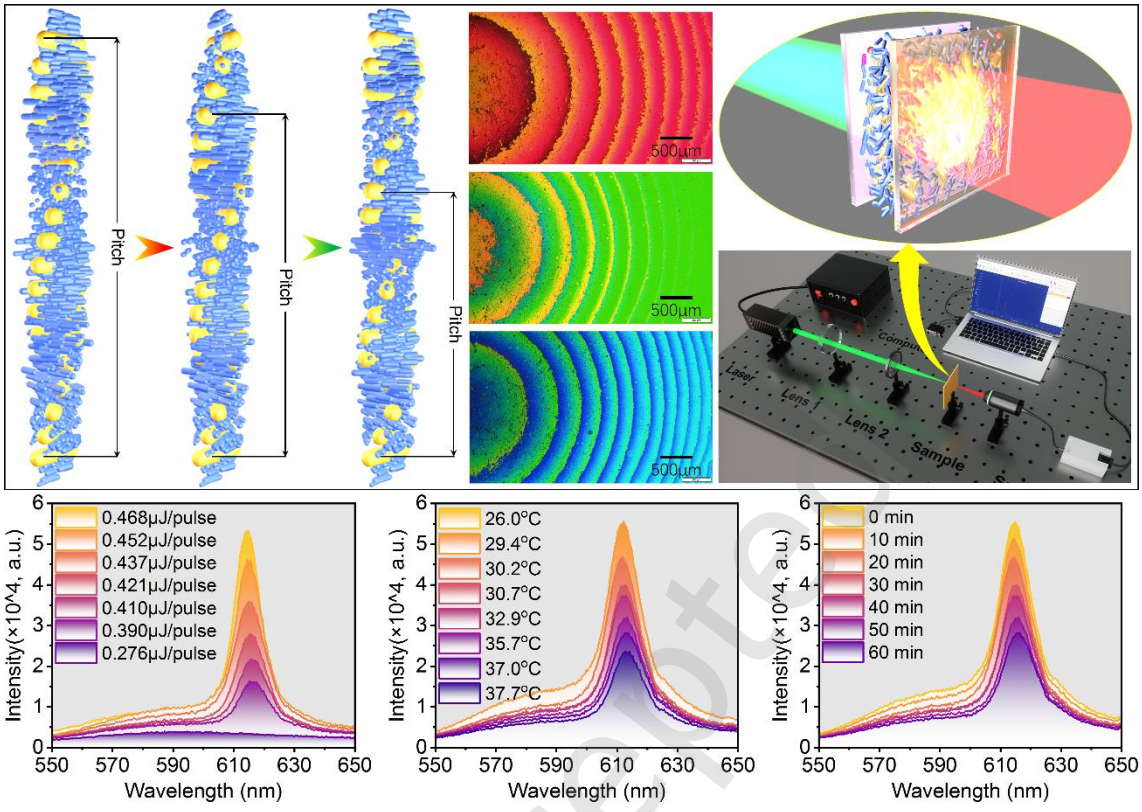

These results validate the successful fabrication of an advanced LC-laser via the integration of an optimized NiO NPs-PVDF alignment layer with a CLC-host containing 0.01 wt% Au NRs. The findings not only suggest the promising utility of gold chiral helical assemblies in LC-lasers but also indicate a viable route for developing future devices with high stability, strong emission, and low pumping-energy consumption.

Nano Research

Open Access

Research Article

Pulsed pumping on piezoelectric PVDF alignment layer suppresses emission consumption of DCM within cholesteric liquid crystal-host

Yang Liu, Chunyang Dai, Xiaohui Gong, Hao Liu, Yongfang Zhang, and Jianhua Shang

School of Information and Intelligent Science, Donghua University, 2999 North Renmin Road, Songjiang District, Shanghai 201620, China

Received: 18 January 2026; **Revised:** 24 April 2026; **Accepted:** 6 May 2026

Address correspondence to Yang Liu, liuyang@dhu.edu.cn; Jianhua Shang, jhshang@dhu.edu.cn

Cite this article: *Nano Research*, 2026, 19, 94908811 https://doi.org/10.26599/NR.2026.94908811

ABSTRACT: Cholesteric liquid crystals (CLCs) doped with dyes have been shown to enable tunable coherent emission, thus forming the basis for versatile liquid crystal (LC)-lasers. However, their practical adoption is hindered by high pumping thresholds and limited long-term stability. This paper proposes a synergistic strategy to overcome these limitations by engineering the alignment layer and the CLC-host. A novel alignment layer based on polyvinylidene-fluoride (PVDF) incorporating NiO nanoparticles (NPs) has been developed. Electro-optical analysis revealed that an 8 wt% NiO NPs-PVDF alignment layer paired with a ZnO-coated slide facilitated highly efficient dipole redistribution, leading to faster switching and a significantly reduced threshold voltage. The integration of the optimized alignment layer with a 0.1wt% gold nanorods (Au NRs) blending CLC-host has enabled the successful fabrication of an advanced LC-laser. The helical assembly of plasmonic Au NRs has been demonstrated to enhance the localized optical field under pumping conditions, thereby achieving a 197% enhancement in DCM emission efficiency. Furthermore, the helical assemblies have been shown to result in a substantial improvement in thermal-dependent quenching of 9.35%. This synergistic approach, which combines a functionalized alignment layer with a plasmonic CLC-host, represents a significant advancement in the development of practical, low-threshold, and highly stable LC-lasers.

KEYWORDS: gold nanorod, cholesteric liquid crystal, polyvinylidene-fluoride (PVDF), chirality, liquid crystal-laser

1 Introduction

Liquid crystal-laser (LC-laser) has emerged as one of significant electro-optic device for sensing, display and optical communication [1-3]. The operational principle of LC-lasers primarily relies on the overlap between the photonic bandgap of the LC-host and the fluorescence spectrum of the laser dye [4-8]. Photons emitted by the dye experience Bragg scattering within the periodic structure of the photonic LCs, leading to distributed feedback (DFB) and ultimately resulting in laser emission [9-12]. Moreover, the alignment of the LCs can influence the polarization, wavelength, and direction of the emitted laser beam, enabling dynamic control of laser output [13-15]. While regarding the lasing characteristics and the stability, high-performance LC-lasers remain challenging [16, 17].

In terms of the resonating LCs in lasers, cholesteric liquid crystals (CLCs) and blue phase liquid crystals (BPLCs) have emerged as popular candidates due to their periodic helical structures and selective reflection properties [18-22]. The helical structure of CLCs provides a periodic photonic bandgap (PBG), which facilitates laser emission along the helical axis with circular polarization characteristics. Applying an external electric field or varying the temperature alters the molecular arrangement, shifting the position and width of the PBG and enabling the wavelength of the laser to be dynamically tuned. Incorporating a polymer matrix and nanomaterials has been identified as an efficient approach to enhancing the performance of LC-lasers regarding emission intensity and stability [23, 24]. Combining the optical properties of CLCs with the mechanical stability of the polymer matrix while retaining efficient laser emission capabilities improves the practicality of LC-lasers for real-world applications [25, 26]. The polymer matrix in polymer-stabilized CLCs (PSCLCs) isolates the CLCs into domains with an ultra-wide blue-phase temperature range of –180°C to 390°C [27]. This has paved the way for LC-lasers that can operate over a broad temperature range of –180°C to 240°C [28], rendering them suitable for use in extreme environmental conditions. Moreover, in addition to the polymer matrix formed to isolate the CLCs, the incorporation of silver nanoflakes into the CLCs has been demonstrated to efficiently improve the emission properties of such an LC-laser due to their intrinsic super localized surface plasmon resonance (LSPR) and the resulting multiple reflections within the hybrids [29]. Furthermore, the blended nanoparticles, such as TiN nanoparticles [30], NiO//ZnO hetero-structured nanoparticles [31] and gold nanocages [32] have been shown to maintain long-term emission stability against 4-(Dicyanomethylene)-2-methyl-6-(4-dimethylaminostyryl)-4H-pyran (DCM) quenching due to their synergistic interactions. In addition to the work towards the resonating LCs in the lasers, the provision of functional layers to LC-lasers has been demonstrated as a viable alternative. GaN alignment layer in cell has been demonstrated to improve the reflectivity and enhance the damage resistivity of the resulting devices [33], and MXene nanostructured thin film has been shown to greatly alter the reflective and display properties of BPLCs [34]. Moreover, the multi SiO_2/TiO_2 dielectric layers

employed in the LC-laser induce the dramatic increase of the photon density of state at the band edges of CLCs [35], and therefore improves the lasing performance by means of band-edge excitation at high-energy band edges.

Laser-induced modulation of the crystalline phase and dipole orientation in polyvinylidene fluoride (PVDF) alignment layers indirectly affects their dielectric properties and alters the pumping environment for blended luminescent dyes in CLCs [36]. In this study, PVDF layers are used to sandwich CLCs forming a resonant cavity designed to enhance and modulate the emission of luminescent dye-DCM. The dielectric and piezoelectric properties of the PVDF films are further tuned by doping with p-type ZnO and n-type NiO nanoparticles (NPs) [37-38]. The generation of an internal electric field and its synergistic interaction with the external electric field are demonstrated through electro-optical switching studies of the sandwiched LCs in the cell, which thereafter reveals the possible reduction in the energy required to pump the DCM to emit. Regarding the emission of DCM in such systems, the pumping threshold, pitch-dependent emission characteristics and emission stability are the focus of intensive investigation.

2 Experimental

1. Preparation of NiO and ZnO Thin Films via Sol–Gel Method: Deposition solutions for NiO and ZnO thin films were prepared using a sol–gel process. For the NiO solution, 6.221 g of $Ni(CH_3COO)_2 \cdot 4H_2O$ was dissolved in 60 mL of 2-methoxyethanol in a thoroughly cleaned reagent bottle. Then, 10 drops of ethanolamine were added as a stabilizer via pipette. The mixture was magnetically stirred at 60 °C for 2.5 hours and aged at room temperature for 24 hours before use. The ZnO solution was prepared analogously: 0.636 g of $Zn(CH_3COO)_2 \cdot 2H_2O$ was dissolved in 32 mL of 2-methoxyethanol in a separate sterile reagent bottle, followed by the addition of 1 mL of ethanolamine measured with a graduated cylinder. This solution was stirred at 70 °C for 2 hours and similarly aged for 24 hours.

2. Preparation of PVDF-Based Composite Thin Films: PVDF, ZnO, and NiO powders were purchased from Sigma-Aldrich and used as received. A PVDF solution was prepared by dissolving PVDF in DMF at a concentration of 1 mg/mL under ultrasonication. ZnO NPs doped PVDF and NiO NPs doped PVDF composite solutions were obtained by blending the PVDF solution with ZnO or NiO powder at concentrations of 2, 4, 6, and 8 wt%, respectively. Each mixture was sonicated for 2 hours to ensure homogeneity.

Glass slides and ITO-coated glass slides were cleaned by sequential washing in acetone, isopropanol, and ethanol for 10 minutes each, then dried in an oven at 60 °C for 30 minutes. A subsequent hydrophilic treatment was performed using a digital ultraviolet ozone system (PSD UV 12, Novascan Technologies, USA) for 30 minutes.

Both NiO and ZnO solutions were spin-coated onto glass slides at 800 rpm for 30 seconds, followed by 2000 rpm for 120 seconds. The coated slides were prebaked at 80 °C for 30 minutes and then annealed in a muffle furnace at 500 °C for 12 hours. The PVDF composite solutions were spin-coated onto the cleaned substrates using the same two-step spin-coating procedure as above. The films were prebaked at 80 °C for 30 minutes and hard-baked at 230 °C for 2 hours.

3. Preparation of Resonating CLC-hosts: CLCs were formulated by blending a chiral dopant (S811, 95%, Hebei Co., Ltd., China) with the nematic LC-E7 at a mass ratio of 29.1:70.9. To incorporate Au nanorods (NRs), an Au NRs solution in CH_2Cl_2 (5 mg/mL) was added to the CLC-host at concentrations of 0.02, 0.05, and 0.1 wt% under sonication. The mixtures were heated at 60 °C for 4 hours to remove residual solvent. For subsequent laser-related experiments, 1.0 wt% of DCM dye was doped into both pure CLC-host and Au NRs blending CLC-hosts, followed by sonication to ensure uniformity.

4. Device Fabrication: The coated slides were unidirectionally rubbed with flannel cloth. LC-cells were constructed using two slides arranged in either anti-parallel or twisted nematic (TN) configuration with aligned rubbing directions. Cell gaps were maintained at 5 μm for anti-parallel and 10 μm for TN cells. The LCs and resonating CLC-hosts were then capillary-filled into the assembled cells for subsequent characterization.

5. Characterization: The optical transmission of thin films was measured using a UV–vis spectrophotometer (Shimadzu UV-3600). Surface morphology was examined by field-emission scanning electron microscopy (FE-SEM, Hitachi S-4800). Contact angles of deionized (DI) water and diiodomethane were measured via the sessile drop method using a contact angle analyzer.

Alignment of LCs was verified with a polarized optical microscope (POM, Olympus BX53P). The threshold voltage and response time of the LC cells were characterized using an LC performance testing system (ALCT-EO1S, Instec, USA) with a step bias voltage of 0.2 V up to a maximum of 5 V. Photocurrent in cells under illumination was detected with a Keithley 4200 Semiconductor Characterization System.

Thermally induced changes in the PBG of the CLC-hosts were investigated using a precision temperature controller (TST350, Linkam, UK; accuracy ±0.1 °C) integrated with the POM. Reflection spectra were recorded during dynamic heating at 1 °C/min using a spectrometer (Ocean Optics USB2000+). Emission from DCM in the CLC-hosts was evaluated using a custom optical setup wherein a pulsed laser (532 nm, 10 Hz, DPS-532-A-1mJ, Changchun New Industries Optoelectronics Technology Co., Ltd., China) pumped the cell, and the emission signal was collected with the same spectrometer.

6. COMSOL Simulations: The power radiation distribution of a point dipole inside a photonic cavity is simulated using the finite element method employing the wave optics module of COMSOL Multiphysics software. The refractive indexes of Au-NCs, C-NCs, DCM and CLCs are 0.27, 1.58, 1.59 and 1.63 respectively.

3 Results and discussion

Due to its polymer nature and agglomerates of molecules, dots and strips were observed from PVDF alignment layer in SEM image as shown in Figure 1a. The incorporation of ZnO NPs and NiO NPs boosts the phase separation and due to the additional agglomeration between NPs, the observed dots and strips become much obvious. Moreover, these observed signs got additional apparent when the blending concentration of NPs progressively increased. In addition to the surface topology change caused by incorporation of NPs, the surface wettability

was found to be tuned accordingly. The surface hydrophilicity and hydrophobicity of PVDF alignment layers were characterized by measuring the contact angles of DI water and diiodomethane droplets. As shown in Figure 1b,c, the contact angle of DI water droplets on a pure PVDF alignment layer is approximately 32.80° initially, while the contact angle decreases progressively when nanoparticles were progressively blended into PVDF alignment layers. Specifically, a contact angle approximately 20.60° has been observed on an 8 wt% ZnO NPs-PVDF alignment layer, and a contact angle approximately 20.95° has been observed on an 8 wt% NiO NPs-PVDF alignment layer. Regarding the contact angle of diiodomethane droplets on the PVDF alignment layers, it was found that initial contact angle was approximately 33.80°, and similarly, when the blending concentration of NPs increased up to 8 wt%, the contact angle on 8 wt% ZnO NPs-PVDF alignment layer was approximately 45.35°, on 8 wt% NiO NPs-PVDF alignment layer was approximately 47.74°. It could be seen that the blending of NPs in PVDF alignment layer has resulted in the increase in hydrophilicity, and therefore contributes to the surface energy enhancement. As shown in Figure 1d,e, the surface energy of an 8 wt% NiO NPs-PVDF alignment layer and an 8 wt% ZnO NPs-PVDF alignment layer was determined as 71.05 mJ/m2 and 71.64 mJ/m2, respectively, which indicates an increase by 5.81% and 6.69% in comparison to the polyimide alignment layer (67.15 mJ/m²). The enhanced surface energy is believed to promote the interactions between the PVDF alignment layers and LCs when they are used as alignment layers, and thus modulating the electro-optical performance of the resulting devices. Even though the blending of NPs in PVDF alignment layers caused the modification of surface morphology as well as the surface wettability of PVDF alignment layer, the optical transmittance of the NPs-PVDF alignment layers still maintained at a significant high level. As shown in Figure 1f,g, the NiO NPs-PVDF alignment layers and ZnO NPs-PVDF alignment layers exhibit the approaching transmittance as pure PVDF over 90% regardless of the blending concentration up to 8 wt%.

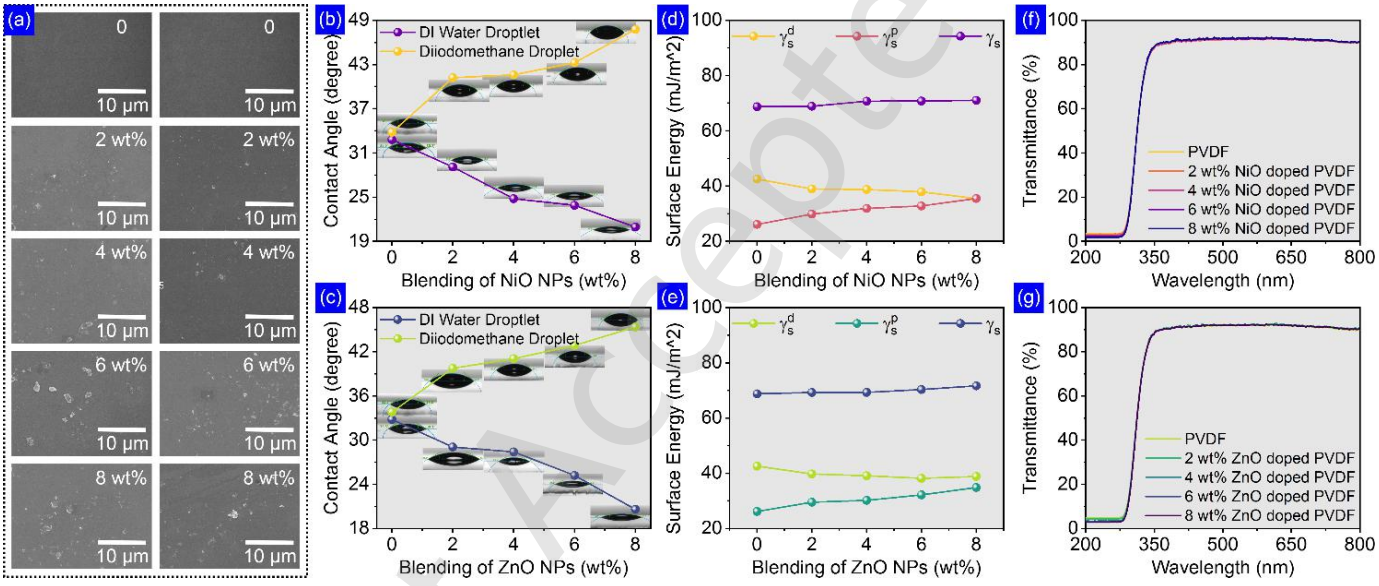

Figure 1 (a) is the SEM image of NiO NPs-PVDF alignment layers and ZnO NPs-PVDF alignment layers. (b) and (c) indicates the contact angles of DI droplet and diiodomethane droplet on NiO NPs-PVDF alignment layers and ZnO NPs-PVDF alignment layers. (d) and (e) are calculated surface energy based on the observed contact angles. (f) and (g) are the optical transmittance of the resulting hybrid alignment layers.

The antiparallel cells were fabricated using NiO NPs-PVDF alignment layer coated slides and ZnO alignment layer coated slides, and ZnO NPs-PVDF alignment layer coated slides and NiO alignment layer coated slides after being rubbed in a P-N junction manner. As shown in Figure 2a,b, LCs in NiO NPs-PVDF//ZnO cells and ZnO NPs-PVDF//NiO cells were homogenously aligned without any observed light leakages, indicating the foundation of their dynamical switch. Thereafter, the cells were additionally fabricated in TN manner, and the threshold voltage of cells were examined as shown in Figure 2c-h. The threshold voltage driving PVDF//ZnO cell using a forward bias to achieve a 10% transmittance has been determined as 1.371V as shown in Figure 2c and Table S1, equaling to 0.274 V/μm. The incorporation of NiO NPs into PVDF alignment layer resulted in a decrease in threshold voltage in progress. When 8 wt% NiO NPs were incorporated into PVDF alignment layer, the resulting 8 wt% NiO NPs-PVDF//ZnO cell exhibited a threshold voltage of 0.972 V, equaling to 0.194 V/μm, which is a decrease about 29.10% in comparison to that of PVDF//ZnO cell. When the forward bias was switched by a reverse bias, it was found that the threshold voltage increased a lot as shown in Figure 2d and Table S1. The threshold voltage of the PVDF//ZnO cell under reverse bias driving was 1.444 V and 0.289 V/μm, in comparation to the forward bias driving, which exhibits an increase about 5.32% as shown in Figure 2e and Table S1. the progress decrease in threshold voltage by incorporation of NiO NPs into PVDF was again observed, and the threshold voltage of the 8 wt% NiO NPs-PVDF//ZnO cell under reverse bias driving has been determined as 1.099 V and 0.220 V/μm, which is a decrease by 23.89% in comparison to that of PVDF//ZnO cell and approaches to the decrease observed under the forward bias driving.

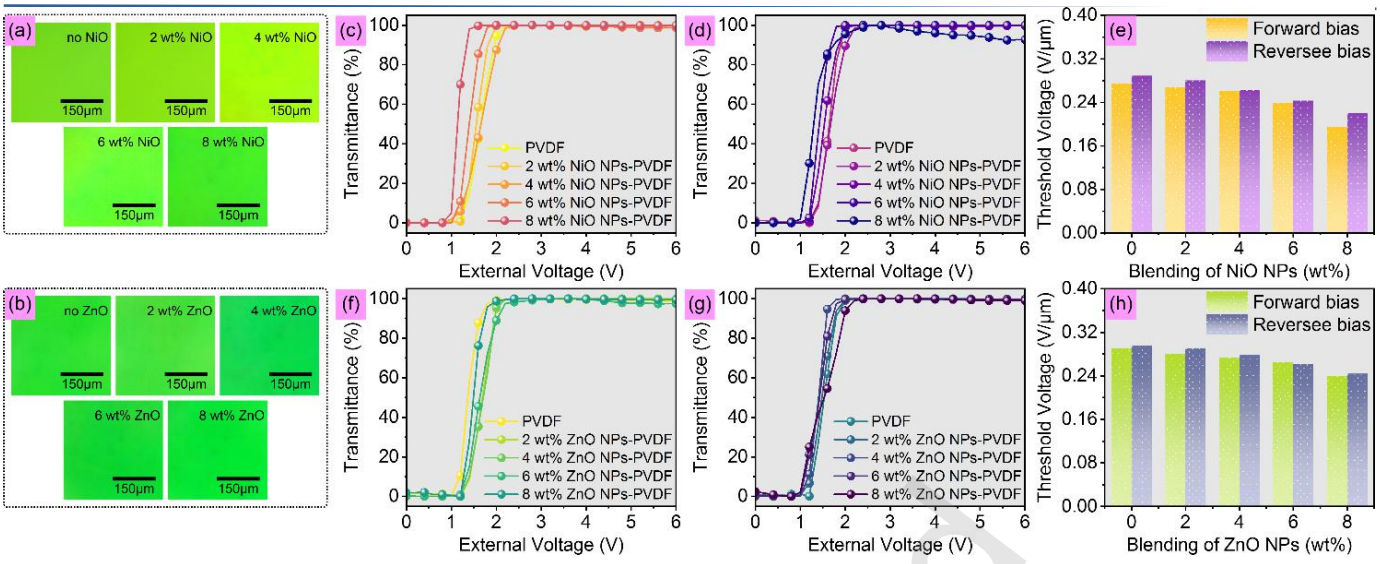

Figure 2 (a) and (b) are POM images of LCs in NiO-PVDF//ZnO and (d-f) ZnO-PVDF//NiO antiparallel cells, respectively. (c,d) and (f,g) are the characterized transmittance-voltage curves of TN cells obtained under the forward bias and reverse bias, and (e) and (h) reveal the comparation of threshold voltage between the forward bias and reverse bias.

The threshold voltage driving PVDF//NiO cell using a forward bias as shown in Figure 2f and Table S2 to achieve a 10% transmittance has been determined as 1.448 V, equaling to 0.290 V/μm. The incorporation of ZnO NPs into PVDF alignment layer similarly resulted in a decrease in threshold voltage in progress. When 8 wt% ZnO NPs were incorporated into PVDF alignment layer, the resulting 8 wt% ZnO-PVDF//NiO cell exhibited a threshold voltage of 1.198 V, equaling to 0.240 V/μm, which is a decrease about 17.27% in comparison to that of PVDF//NiO cell. When the forward bias was switched by a reverse bias, it was found that the threshold voltage increased a lot as shown in Figure 2g and Table S2. The threshold voltage of the PVDF//NiO cell under reverse bias driving was 1.474 V and 0.295 V/μm, in comparison to the forward bias driving, which exhibited an increase about 1.80% as shown in Figure 2h and Table S2. The progressive decrease in threshold voltage by incorporation of ZnO NPs into PVDF was again observed, and the threshold voltage of the 8 wt% ZnO NPs-PVDF//NiO cell under reverse bias driving has been determined as 1.219 V and 0.244 V/μm, which is a decrease by 17.30% in comparison to that of PVDF//NiO cell and approaches to the decrease observed under the forward bias driving. These observations indicate that the pairing between NiO NPs-PVDF alignment layer coated slide with ZnO coated slides is of significant advantage in achieving a lower consumption LC-cell, especially when the cell is subjected to a forward bias.

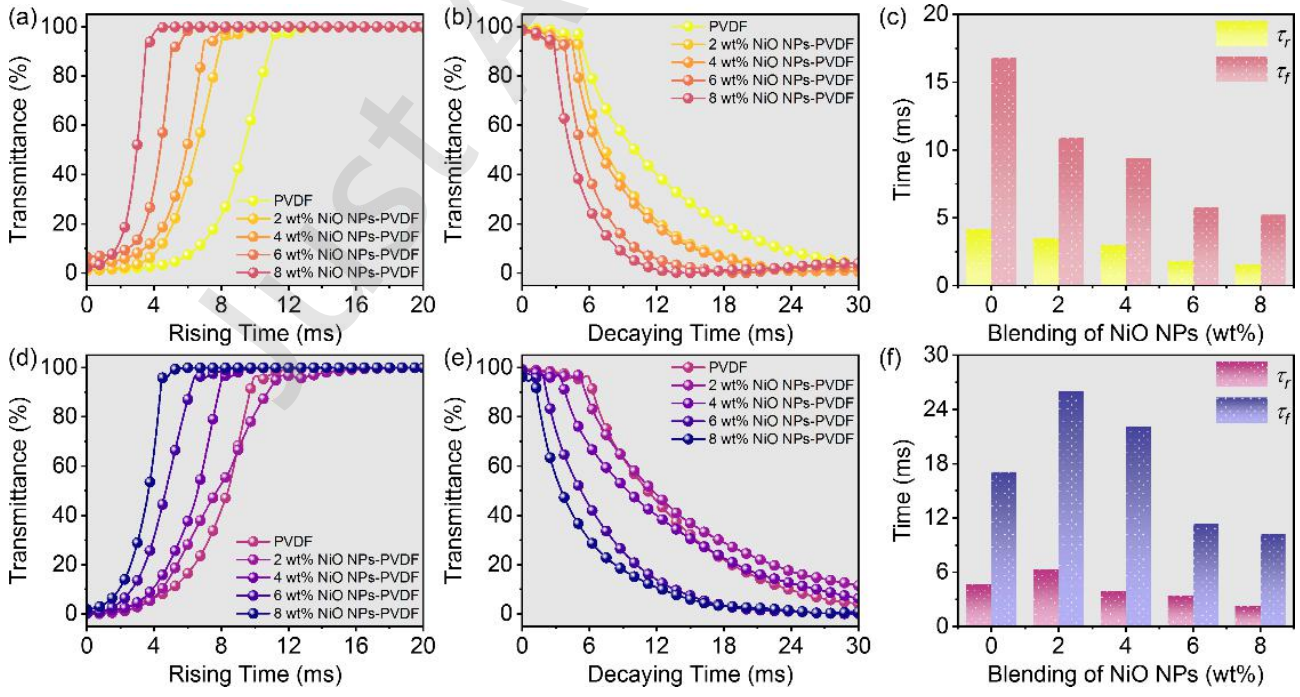

Figure 3 (a-c) is the rising time and decaying time of LCs in NiO NPs-PVDF//ZnO cells under a forward bias, and (d-f) is under a reverse bias.

Thereafter, the switching of LCs within the NiO NPs-PVDF//ZnO cells was investigated and characterized in an "on" period and an "off" period in terms of response time. The response time of LCs driven under the forward bias is shown in Figure 3a-c and Table S1, it could be seen that the rising time that defined as the period getting transparency from 10% to 90% decreased progressively in response to the incorporation of NiO NPs into PVDF alignment layer. The rising time of LCs in pure

PVDF//ZnO cell initially has been characterized as 4.143ms, and this rising time decreased to 3.476 ms, 2.987 ms, 1.830 ms and 1.596 ms, respectively, when 2 wt%, 4 wt%, 6 wt% and 8 wt% NiO NPs were incorporated into PVDF alignment layer, respectively, as indicated in Figure 3a and Table S1. It is noteworthy that the incorporation of NiO NPs into the PVDF alignment layer resulted in a significant decrease of approximately 61.48% in rising time. Furthermore, the accelerated decaying time of LCs when the external voltage was removed was also observed. The decaying time of LCs in pure PVDF//ZnO cell has been characterized as 16.816 ms. The decaying time of LCs in pure PVDF//ZnO cell has been characterized as 16.816 ms, and this decaying time decreased to 10.921 ms, 9.377 ms, 5.775 ms and 5.227 ms when 2 wt%, 4 wt%, 6 wt% and 8 wt% NiO NPs were incorporated into PVDF alignment layer, respectively, as indicated in Figure 3c and Table S1. The incorporation of NiO NPs into a PVDF aslignment layer resulted in a significant reduction in decay time, with a reported decrease of approximately 68.92%.

While, when the cell was subjected to a reverse bias, the response time in both the on period and the off period increased considerably as shown in Figure 3d-f and Table S1. The rising time of LCs in pure PVDF//ZnO cell has been characterized as 4.634 ms. This rising time decreased to 4.286 ms, 3.893 ms, 3.440 ms and 2.301 ms when 2 wt%, 4 wt%, 6 wt% and 8 wt% NiO NPs were incorporated into the PVDF alignment layer, respectively, as shown in Figure 3d and Table S1. The incorporation of NiO NPs into PVDF alignment layer resulted in a decrease of approximately 2.333 ms in rising time, representing a reduction of 50.35%. Furthermore, the accelerated decaying time of LCs when the external voltage was removed was also observed. The decaying time of LCs in pure PVDF//ZnO cells has been characterised as 17.094 ms, and this decaying time decreased to 25.976 ms, 22.083 ms, 11.372 ms and 10.231 ms when 2 wt%, 4 wt%, 6 wt% and 8 wt% NiO NPs were incorporated into PVDF alignment layer, respectively, as shown in Figure 3e and Table S1. The incorporation of NiO NPs into the PVDF alignment layer resulted in a decrease of approximately 6.863 ms in decay time, corresponding to a 40.15% reduction

The observed reduction in threshold voltage and accelerated response of the LCs under forward bias, compared to reverse bias, can be attributed to the gain of coupling between the light field and the external electric field. As shown in Figure 4, the photogenerated currents in the cells under illumination were measured using an automated semiconductor characterization system. The photocurrent increased significantly with increasing blending concentrations of NiO NPs, and nearly doubled at 8 wt% NiO NPs in the PVDF alignment layer relative to the PVDF//ZnO reference cell. NiO NPs are well-established photon hunting semiconductor material [39], the interaction between light and NiO promotes dipole movement and consequently induces an internal electric field, which couples with the forward external field to lower the required threshold voltage to switch LCs.

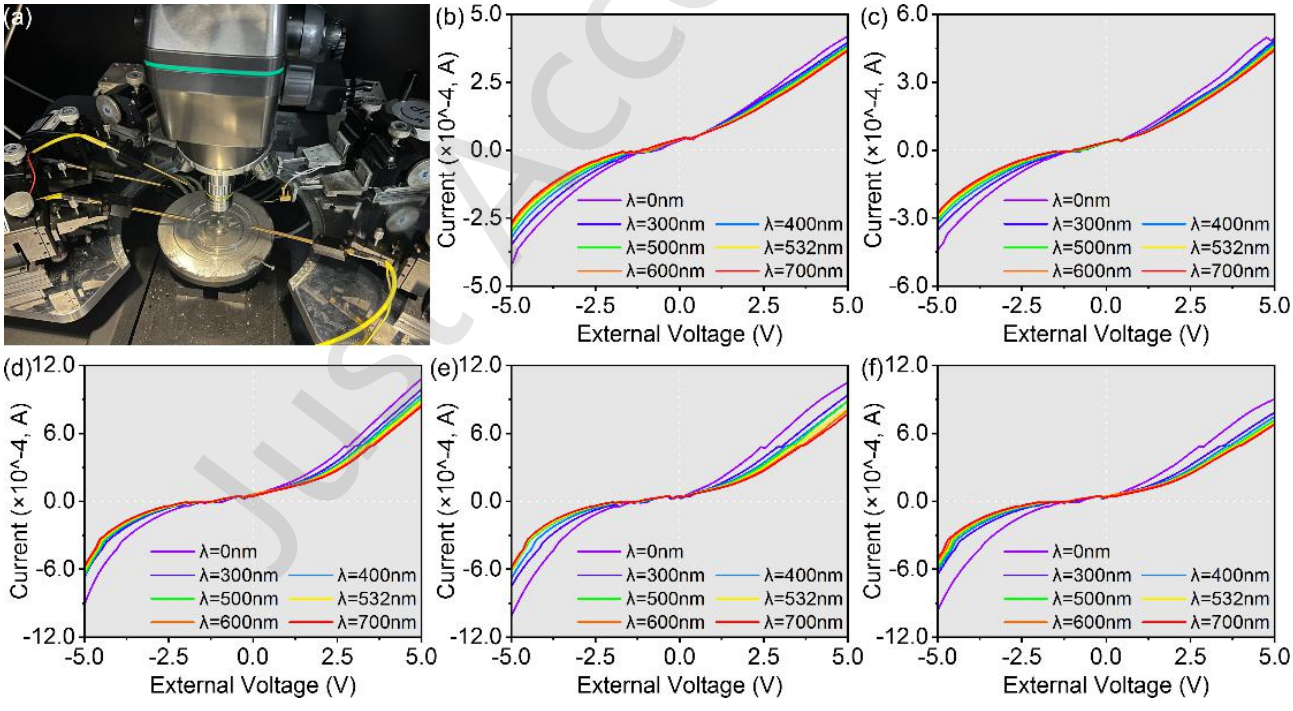

Figure 4 The I-V curves of NiO NPs-PVDF//ZnO cells subjected to light illumination at various wavelengths. The blending concentration of NiO NPs in PVDF alignment layer is (a) 0 wt%, (b) 2 wt%, (c) 4 wt%, (d) 6 wt% and (e) 8 wt%, respectively.

CLCs in LC-laser have been demonstrated to facilitate the modulation of the amplitude and phase of incident light and emission signal. Herein, CLCs were injected into NiO NPs-PVDF//ZnO cells, and the reflection of incident subjected to thermal stimuli was investigated as shown in Figure S1 and Figure 5a-d. It could be seen that the thermal induced reflection under POM observation went a blueshift by increasing the heating temperature, and the reflection exhibits a transition from red at 29.2 °C to violet at 37.5 °C progressively. This thermal induced progressive refraction has been additionally revealed in the reflection spectra, and it was labeled that the blending of NiO NPs in PVDF alignment layers resulted in the reflection enhancement in the UV wavelength range. This enhancement is due to the intrinsic reflection difference between PVDF and NiO NPs. The chromaticity diagram as shown in Figure 5e further provides a visual representation of the chromaticity coordinates

and the variations caused by NPs blending. The triangle vertexes were found to be (0.27, 0.31), (0.35, 0.42), and (0.40, 0.31) for CLCs in PVDF//ZnO cell coordinates. Incorporation of NiO NPs into PVDF alignment layers has been shown to result in a reduction of the reflection triangle. The vertexes of the triangular configuration of the CLCs in the 4 wt% NiO NPs-PVDF//ZnO cell shifted to (0.27, 0.35), (0.37, 0.42), and (0.40, 0.32), and in the 8 wt% NiO NPs-PVDF//ZnO cell finally shifted to (0.20, 0.30), (0.31, 0.32), and (0.39, 0.41).

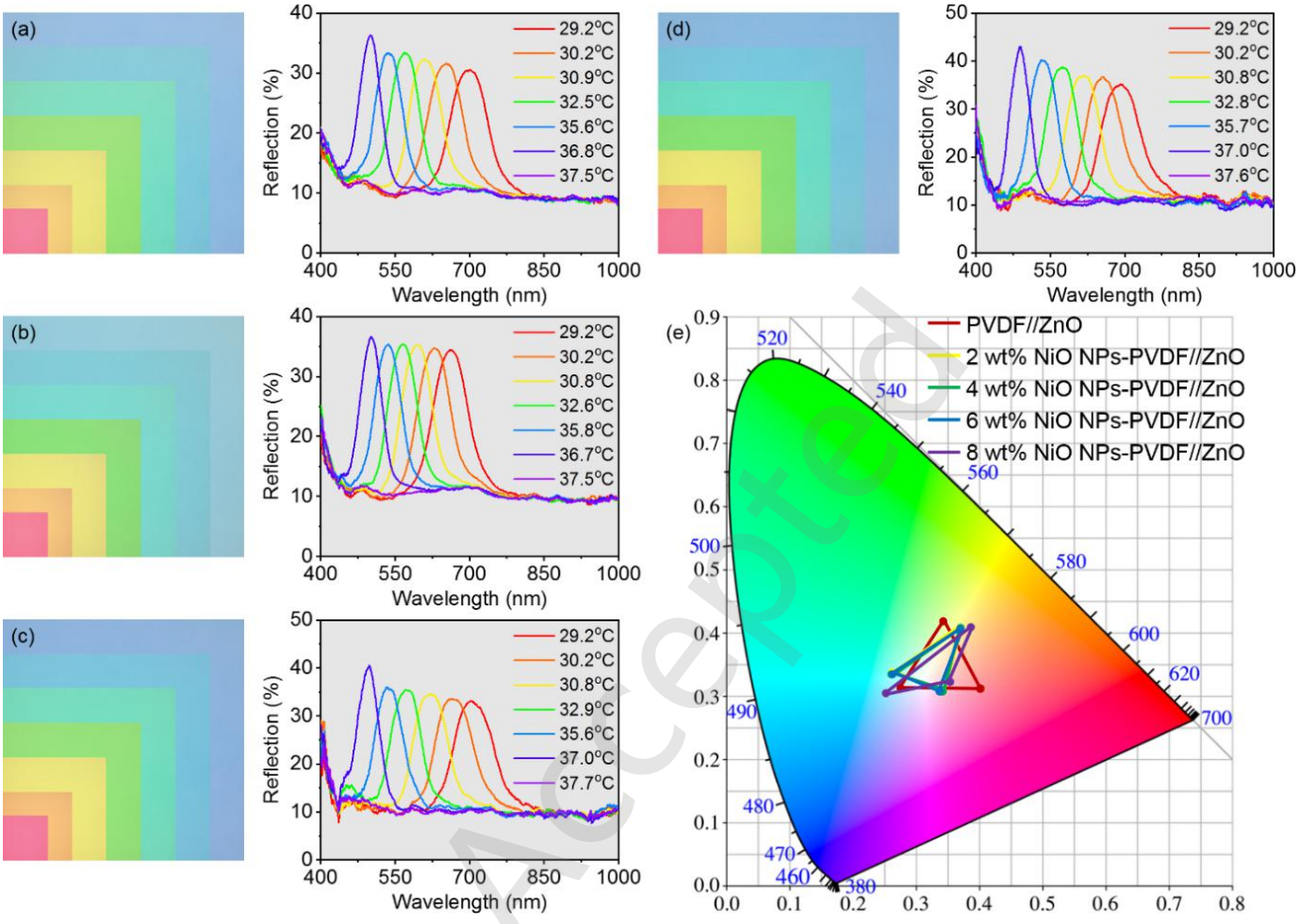

Figure 5 (a-d) are POM images and the corresponding dynamic reflectance spectra of CLCs in NiO NPs-PVDF//ZnO cells subjected to thermal stimuli at blending concentrations of 2 wt%, 4 wt%, 6 wt% and 8 wt%, respectively, and (e) is the corresponding CIE diagram of the reflection.

A schematic of the optical pumping scheme for DCM within the CLC-host is shown in Figure 6a, with the corresponding device emission shown in Figure 6b. DCM was then doped into the CLCs, which were sandwiched between NiO NPs–PVDF and ZnO alignment layers, and the lasing characteristics were investigated by optically pumping the device through either the NiO NPs–PVDF composite layer or the ZnO layer. The threshold pumping energies for a reference PVDF//ZnO cell to induce DCM emission were measured to be similar 0.359 μJ/pulse as shown in Figure 6c,i, and in case of blending PVDF with NiO NPs, the union between threshold pumping energy maintained. Specifically, with the addition of NiO NPs into the PVDF alignment layer at 2%, 4% 6% and 8%, the threshold energies decreased progressively to 0.348 μJ/pulse (Figure 6d,j), 0.338 μJ/pulse (Figure 6e,k), 0.328 μJ/pulse (Figure 6f,l) and 0.317 μJ/pulse (Figure 6g,m), respectively. Differential efficiency (η) defined as the slope of the laser output power versus the incident pump power [31] and serving as a comprehensive indicator of DCM emission quality, is given by:

$$\eta = \frac{P_E}{P_P - P_{th}}$$

in which P_E is the output emission power of the DCM, P_p is a given pump power above threshold, and P_{th} is the determined threshold pump power. As demonstrated in Figure 6h,n, the mean differential efficiency ($\bar{\eta}$) exhibited a progressive decline with increasing concentrations of NiO NPs. It has been demonstrated that, despite the reduced threshold pumping energy and enhanced emission intensity, the blending of NiO NPs into the PVDF alignment layer introduces certain drawbacks that compromise $\bar{\eta}$. Specifically, the incorporation of 8.0 wt% NiO NPs into the PVDF/ZnO cell resulted in a 13.82% and 10.37% reduction in $\bar{\eta}$ when pumping through the NiO NPs-PVDF and ZnO sides, respectively. Moreover, pumping through the PVDF side exhibited notably higher $\bar{\eta}$ than through the ZnO side indicating asymmetric pumping behavior, and this asymmetry persisted after incorporating NiO nanoparticles into the PVDF layer, which further reduced the lasing threshold.

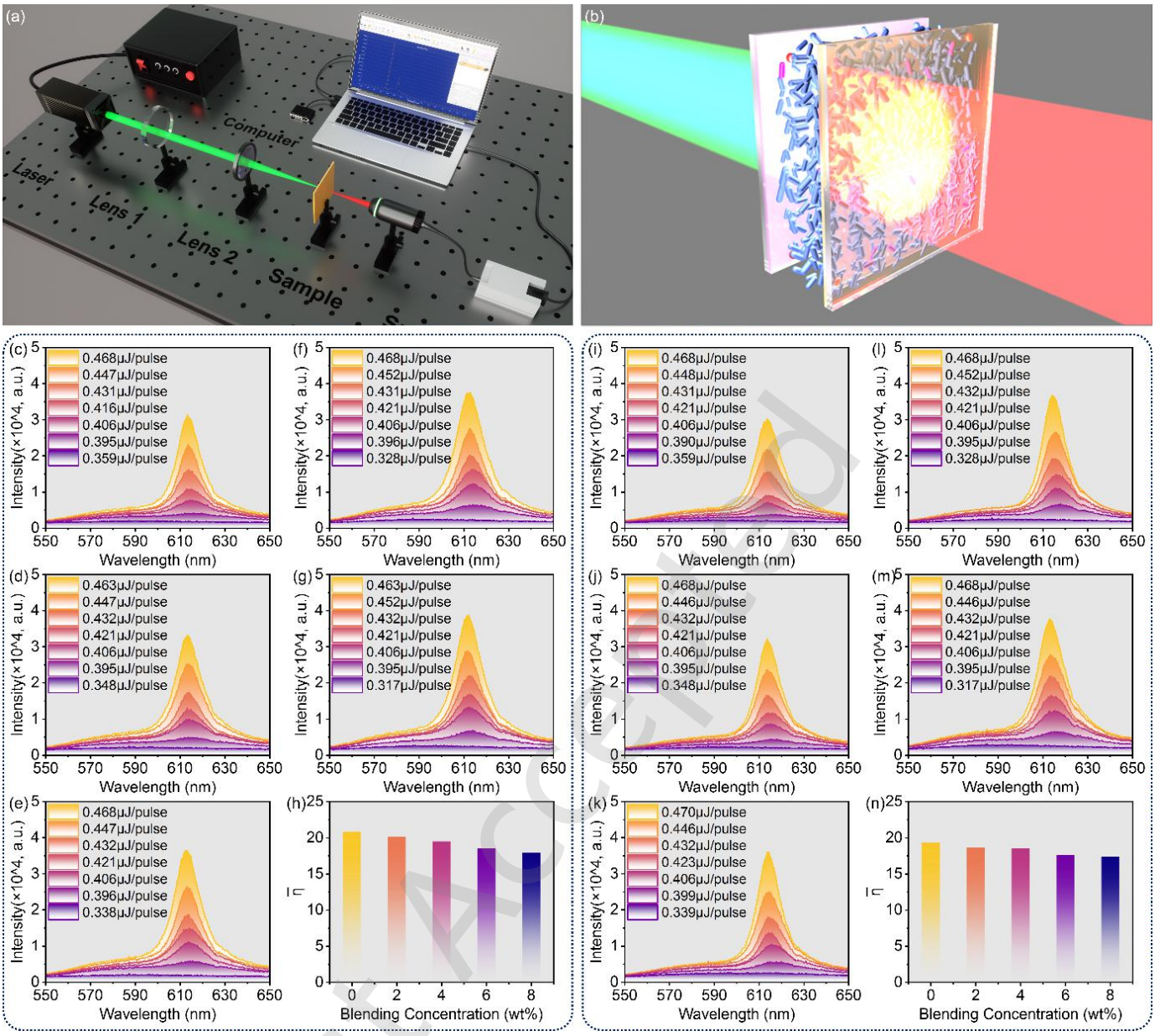

Figure 6 (a) is the schematic indicating the pumping on DCM in CLC-host, and (b) the corresponding emission in cell. (c-g) represent the emission of DCM within the CLC-host in NiO NPs-PVDF//ZnO cells subjected to different pumping energies. The emission of DCM was pumped on NiO NPs-PVDF alignment layer coated glass slide, (i-m) are on ZnO alignment layer coated glass slide, and (h, n) are the calculated η̄, respectively.

It is evident that quenching constitutes the primary cause of emission instability in DCM, and the host and alterations in the host environment have the capacity to induce quenching in DCM. The host-induced degradation, which is predominantly catalyzed by hydrogen bonding, modifies the excited-state behavior of DCM, , resulting in a reduction in emission efficiency. Furthermore, the aggregation of DCM molecules has been observed to impede the process of intramolecular charge transfer, which consequently affects the subsequent reduction in fluorescence intensity. Therefore, the thermally induced quenching of DCM embedded in the CLC-host was studied alongside the variation in the PBG of the CLCs in cells. As shown in Figure 7a, the emission intensity of DCM in the PVDF//ZnO cells decreased progressively as the temperature rose from 26 °C to 37.9 °C, eventually stabilizing at 27.02% of its initial value. After incorporating NiO nanoparticles into the PVDF layer, the thermal quenching of DCM in the resulting NiO NPs-PVDF//ZnO cells was significantly suppressed, with the extent of suppression increasing at higher NiO NP concentrations as shown in Figure 7b-f. Notably, when 8.0% NiO NPs were blended into the PVDF layer, the thermal quenching ratio was limited to 32.13%, accompanied by a decrease in emission intensity from 4.25 to 1.36 as shown in Figure 7e. Regarding the time-dependent quenching behavior, the incorporation of NiO NPs into the PVDF layer also played a notable role in mitigating the quenching process as depicted in Figure 7g-l. Although the DCM emission in the modified cell remained at ~50% of its initial value—similar to that in the PVDF//ZnO cell—the final emission intensity was substantially higher than that in the PVDF//ZnO cell as shown in Figure 7l.

The observed enhancement in both thermal-dependent and time-dependent quenching is primarily ascribed to the improved polarization of dipoles in DCM under optical pumping. On one hand, laser pulse below the ablation threshold locally heats the PVDF alignment layer, altering the dipole orientation of the polar β-phase in PVDF, therefore indirectly modifying the dielectric and piezoelectric properties. The localized switching

of polarization direction in specific regions induces variations in the piezoelectric response and dielectric constant, thereby facilitating dipole re-polarization within the DCM and ultimately boosting the emission efficiency. On the other hand, under photon irradiation, the P–N junction formed at the NiO NPs–PVDF//ZnO interface generates an internal electric field. This field further polarizes the dipoles in the DCM and contributes to the acceleration of emission. The photocurrent in the NiO NPs–PVDF//ZnO cells increases progressively with higher NiO NP blending concentrations under photon irradiation as shown in Figure 4, confirming the establishment of this internal electric field.

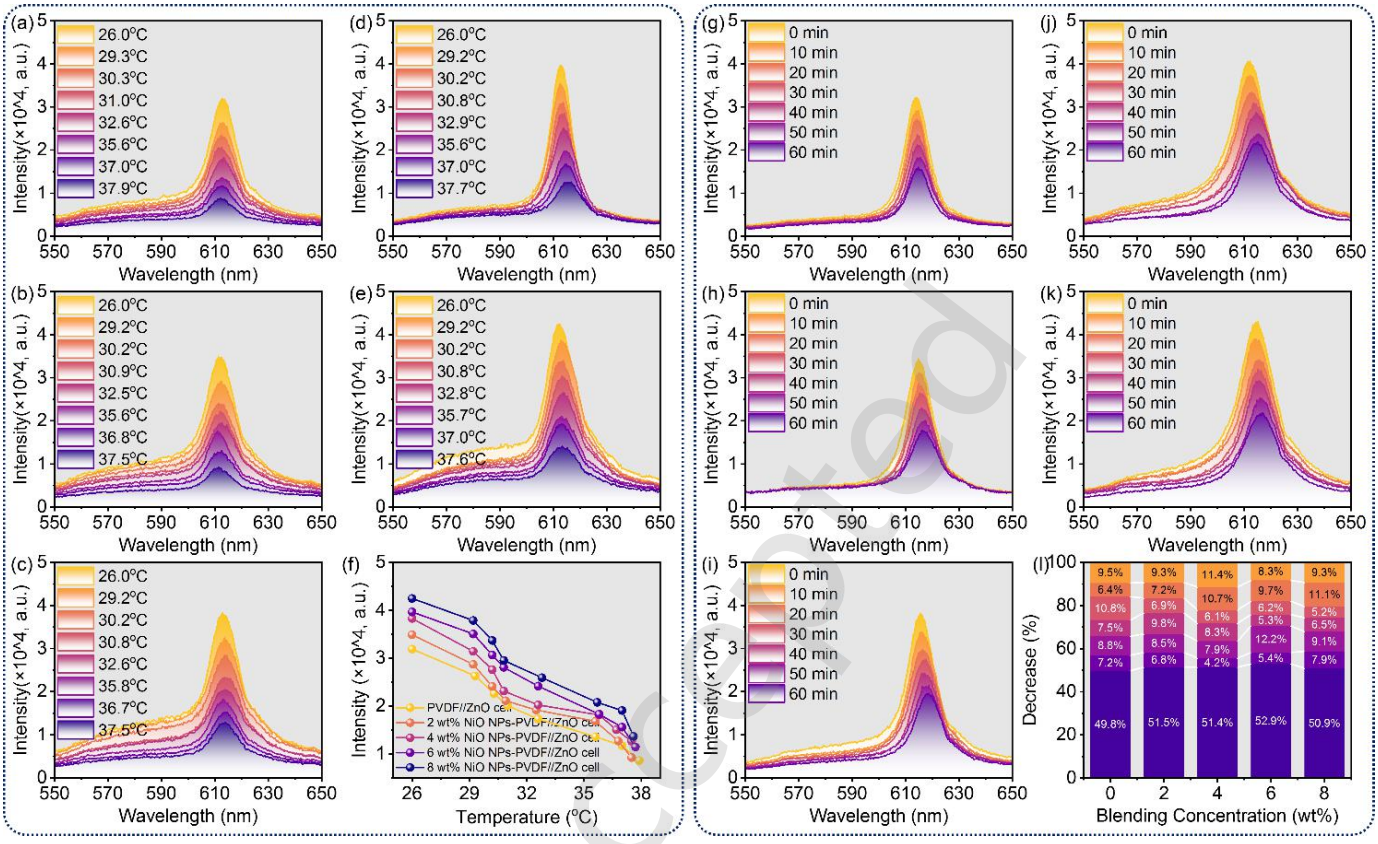

Figure 7 (a-e) are the temperature-luminance characteristics and (g-k) are the time-luminance characteristics over the course of each 10-minute of DCM in NiO NPs-PVDF//ZnO cells. (f, l) are the corresponding summary luminance characteristics. The intensity of the pumping signals was measured at a pump energy of 0.468 μJ/pulse.

The incorporation of Au NRs into CLC-host has been demonstrated to boost the emission of DCM with the deduced pumping consumption and higher emission intensity [6]. Herein, Au NRs were blended with CLCs and inserted into the 8 wt% NiO NPs-PVDF//ZnO cells to improve the performance of LC-laser. The Au NRs incorporated into the CLC-host were firstly characterized by TEM, revealing a well-defined rod-like morphology for each nanorod as illustrated in Figure 8a. By statistically analyzing 394 individual Au NRs, the average diameter and length were determined to be 15 nm and 44.5 nm, respectively (Figure 8b, c). It is proposed that the blended Au NRs in CLC-host align with the LCs and co-assemble into helical assemblies. Upon thermal stimulation, the temperature-dependent interaction strength of the chiral dopant induces reorientation of both the LCs and Au NRs, leading to structural reorganization of the helical assemblies. This reorganization in turn modulates the photonic band gap as illustrated in Figure 8d. Corresponding to the pitch variation under thermal stimuli, the optical reflection of the CLC-host blended with 0.05 wt% Au NRs was monitored and is presented in Figure 8e. A contraction of the central reflection circle and expansion of the outer rings were observed, accompanied by a blueshift in the reflection color. These results collectively confirm the successful chiral co-assembly of Au NRs within the CLC-host.

It could be seen that regardless of the incorporation of Au NRs into CLC-host, the resulting hybrid in 8 wt% NiO NPs-PVDF//ZnO cell exhibits the extremely similar reflection characteristics with the pure CLC-host as shown in Figure S2. The reflection observed under POM indicates that the Au NRs blending CLC-hosts exhibited the blueshift of visuals in responding to the thermal stimuli, as evidenced by the reflection signals. It was also observed that the incorporation of Au NRs into CLC-host enhanced the reflection intensity in vis range as shown in Figure S2a-d. Specifically, the reflection intensity of the signal located at ~500 nm has been determined as 45% for pure CLC-host in the 8 wt% NiO NPs-PVDF//ZnO cell, and the reflection intensity became 48% after the blending of 0.02 wt% Au NRs, 54% by the blending of 0.05 wt% Au NRs, and 60% by the blending of 0.10 wt% Au NRs. In comparison to pure CLC-host, the Au NRs blending CLC-hosts in addition exhibit the enlarged triangular configurations. In specific, the triangular vertexes of triangular configuration that coordinates the pure CLC-host in PVDF//ZnO were (0.20,0.30), (0.31,0.32), and (0.39,0.41) as shown in Figure S2e. When 0.02% Au NRs were blended into CLC-host, the vertexes shifted to (0.25, 0.34), (0.34, 0.29), and (0.37, 0.37); and when 0.02% Au NRs were blended into CLC-host, the vertex shifted to (0.25, 0.34), (0.34, 0.29), and (0.37, 0.37); With the increase of blending concentration of Au NRs up to 0.1 wt%, the vertex finally shifted to (0.25, 0.34), (0.34, 0.29), and (0.37, 0.37).

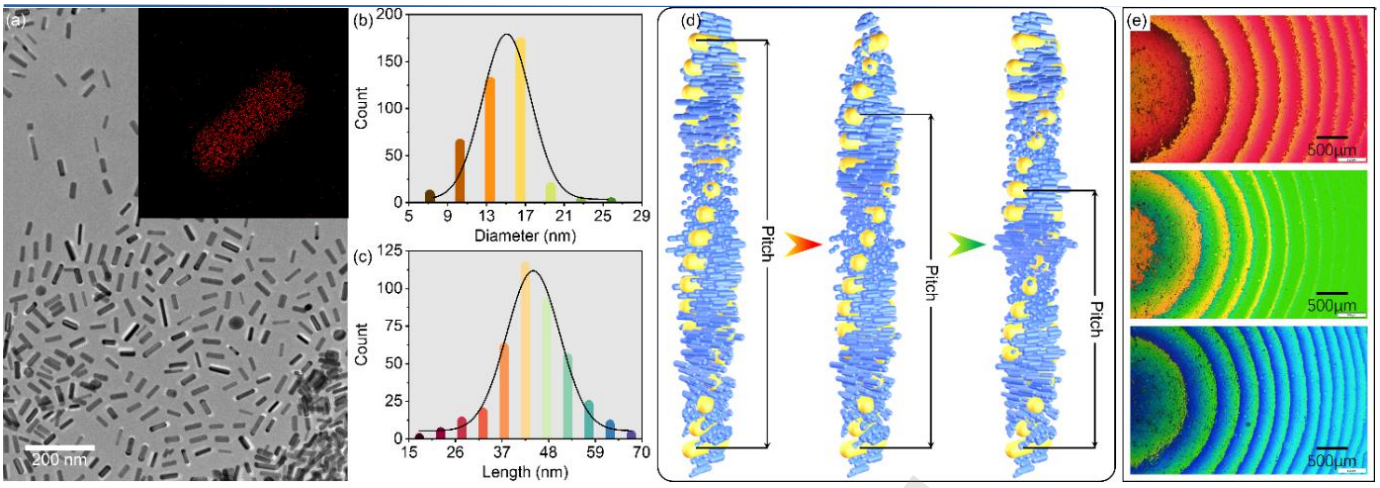

Figure 8. (a) is the representative TEM image of the Au NRs, and (b, c) are histograms showing the distribution of their diameter and length as determined from TEM analysis. (d) is the schematic illustrating the tuned geometry of Au NRs helical assembly within the CLC-host, alongside a corresponding POM image showing the experimentally observed pitch change as indicated in (e).

The threshold pumping energy of DCM in Au NRs-blending CLC-hosts were further investigated. As shown in Figure 9, the pumping threshold of the 8.0 wt% NiO NPs-PVDF//ZnO cell clearly decreased with increasing the blending concentration of Au NRs, accompanied by an amplification of the DCM emission intensity. Compared to the reference CLC-host within 8.0 wt% NiO NPs-PVDF//ZnO, the pumping threshold for DCM in the 0.02 wt% Au NRs-blended CLC decreased to 0.307 μJ, with a reduction of 3.15% as shown in Figure 9b. Further increasing the Au NRs concentration to 0.05 wt% led to a threshold of 0.296 μJ, with a reduction of 6.62%; and at 0.1 wt%, the threshold dropped to 0.276 μJ, corresponding to a 12.93% decrease relative to the pure CLC-host as shown in Figure 9c,d. The incorporation of Au NRs into CLC-host could significantly improve the $\bar{\eta}$ as shown in Figure 9e, and the $\bar{\eta}$ became almost 1.97-times by incorporation of 0.1 wt% Au NRs in comparison to the pure CLC-host.

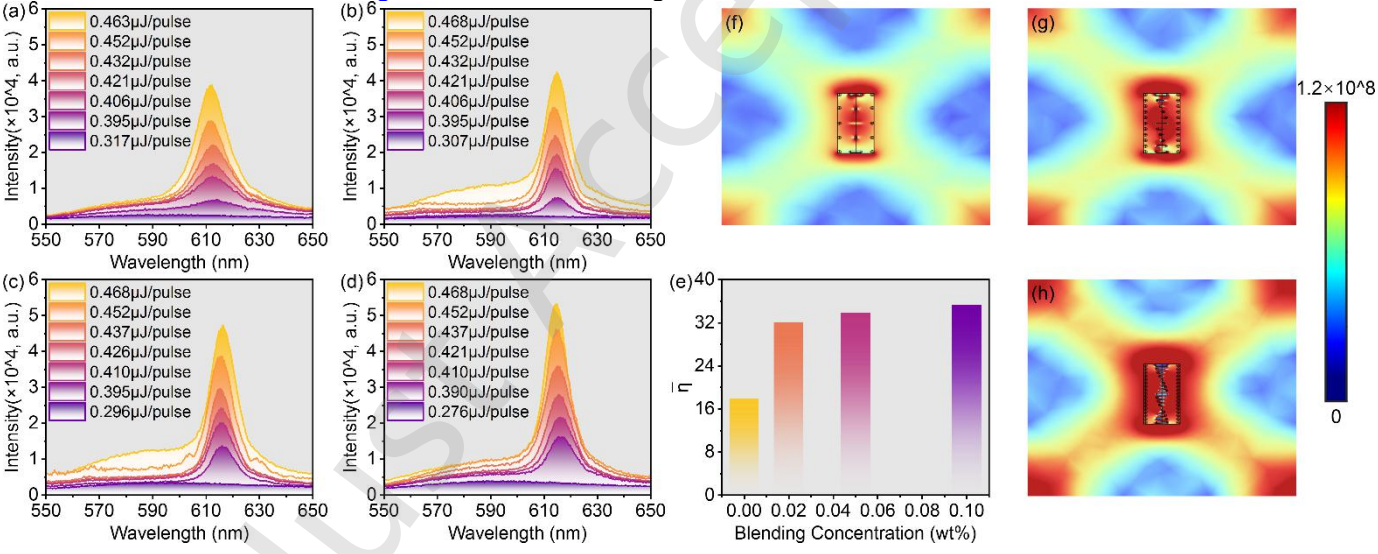

Figure 9 (a-d) are the emission of DCM within the Au NRs blending CLC-hosts in 8 wt% NiO NPs-PVDF//ZnO cells subjected to different pumping energies. The blending concentrations of Au NRs in (a-d) are 0, 0.02 wt%, 0.05 wt% and 0.10 wt%, respectively. (e) is the calculated $\bar{\eta}$ against blending concentration of Au NRs. (f-h) show the evolution of the power radiation profile with increasing Au NRs concentration.

The blending of Au NRs into the CLC-host will lead to significant birefringence. The coupling of Au-NRs with incident light induces oscillations of free electrons on the surface of the nanorods, thereby generating a localized surface plasmon resonance (LSPR) effect. The power radiation distribution of the prepared mixture in the x-y plane was obtained through simulation. The oscillating dipole radiates power in a direction perpendicular to the oscillation direction, and the dipole is located inside the helical assembly. Taking the CLC-host doped with DCM and Au NRs as the main body, the numbers of Au NRs are 5, 11, and 17 respectively. As shown in the simulation results in Figure 9f-h, as the number of Au NRs increases, the radiation emitted by the dipole is significantly enhanced. In addition, as shown in the following equation it can be observed that when Au NRs are stimulated, due to the accumulation of dipoles on the surface, a new local recovery field (LRF) will be generated around Au NRs as indicated in equation (1),

$$\overrightarrow{E^*} = \sum_{k=1}^{N}\sum_{j=1}^{N}\left\{k^2\overrightarrow{a_{jk}}\times\left(\overrightarrow{a_{jk}}\times\overrightarrow{P_k}\right)+\frac{1-ika_{jk}}{a_{jk}^2}\times\left[a_{jk}^2\overrightarrow{P_k}-3\overrightarrow{a_{jk}}\left(\overrightarrow{a_{jk}}*\overrightarrow{P_k}\right)\right]\right\}\times\frac{\exp(ika_{jk})}{a_{jk}^3}\ (j\neq k,\ (1)$$

among them, E^* is the field vector of the dipole at position k at position j, P_k is the polarization vector, and a is the position far from the center of Au NRs. Therefore, the difference between the local recovery field in Au NRs and the electron displacement

leads to an obvious local surface plasmon resonance (LSPR). These observations thus indicate that the blending of Au NRs into the CLC-host amplifies the electromagnetic field intensity in the vicinity of the nanorods, thereby enhancing the absorption and emission capabilities of DCM. Consequently, this process has been shown to increase the absorption and emission efficiency, as well as to enhance emission intensity of DCM.

In addition to the reduced pumping threshold, the incorporation of Au NRs into the CLC-host also improved the emission stability against thermal and time-dependent quenching. When heated from 26 °C to 37.9 °C, the Au NRs-blending CLC-hosts maintained DCM emission longer than the pure CLC-host. Specifically, the final emission intensity of DCM reached 35.54% of its initial value in the 0.02 wt% Au NRs blending as shown in Figure 10b, 39.09% in the 0.05 wt% Au NRs blending CLC-host as shown in Figure 10c, and 41.48% in the 0.10 wt% Au NRs blending CLC-host as shown in Figure 10d. These indicate an increase of 1.06%, 21.66% and 29.10% relative to the thermal-dependent quenching of DCM in the pure CLC-host as indicated in Figure 10e. However, the addition of Au NRs did not significantly suppress the time-dependent quenching of DCM. The emission intensity loss as illustrated in Figure 10f-i was determined as 53.5%, 53.8%, and 50.3% for Au NRs concentrations of 0.02 wt%, 0.05 wt%, and 0.10 wt%, respectively, indicating a similar time-dependent quenching relative to the DCM in the pure CLC-host as shown in Figure 10j. These results demonstrate that the blending of Au NRs into the CLC-host not only enhances the pumping efficiency of DCM but also provides an effective strategy for sustaining emission under thermal and temporal quenching conditions.

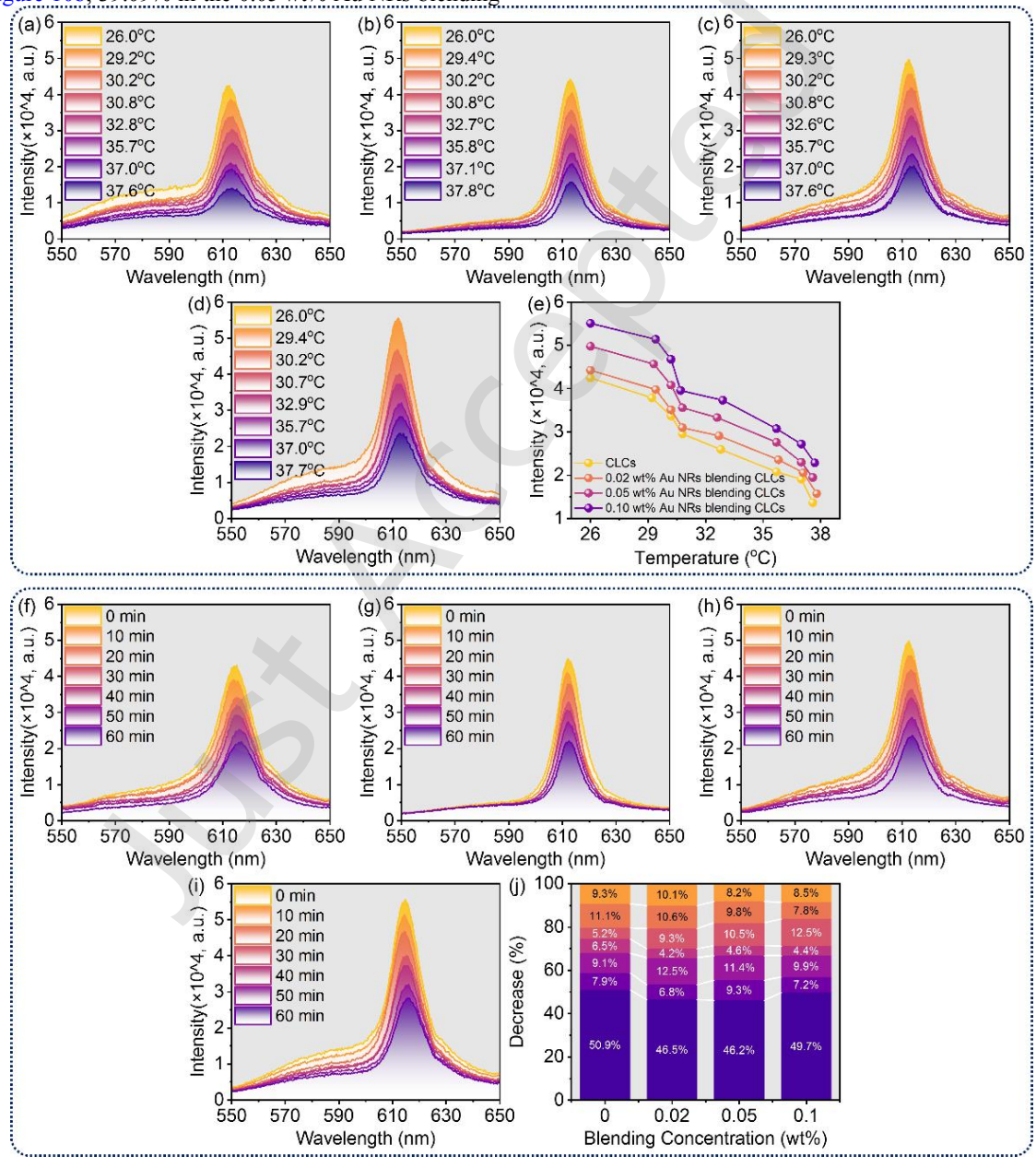

Figure 10. (a-d) are the temperature-luminance of DCM within the Au NRs blending CLC-hosts in 8 wt% NiO NPs-PVDF//ZnO cells, and (f-i) are the time-luminance characteristics over the course of each 10-minute. (e, j) are the summary luminance characteristics. The intensity of the luminance signals was quantified at a pump energy of 0.468 μJ/pulse.

4 Conclusions

In summary, this study demonstrates a synergistic strategy that combines functionalization of the alignment layer with enhancement of the photonic properties of the CLC-host to improve the emission performance of blended dyes for laser

applications. The alignment layer was modified by incorporating NPs into the PVDF alignment layer. SEM confirmed the homogeneous dispersion of NPs within the PVDF matrix, and the resulting composite alignment layers exhibited surface energy and optical transparency comparable to those of pure PVDF. When comparing the electro-optical performance of LCs in the NiO NPs-PVDF//ZnO cell against those with ZnO NPs-PVDF//NiO cell under forward bias, the former exhibited a lower threshold voltage and faster response. This behavior is mainly attributed to the formation of a P–N junction between the layers. The application of an external electric field induces an internal field that superimposes with the external one, thereby reducing the required driving voltage. The presence of this synergistic internal electric field was verified by photocurrent measurements across the P–N junction under illumination. Optimization revealed that a doping concentration of 8 wt% NPs most effectively strengthened the internal field, achieving a threshold voltage as low as 0.324 V/μm, along with rise and decay times of 2.67 ms and 4.89 ms, respectively. Consequently, the 8 wt% NiO NPs-PVDF//ZnO cell was selected for fabricating the LC-laser. The CLC orientation within the cell was minimally affected by NP doping in the PVDF alignment layer, preserving the tunability of the photonic band gap. Moreover, reflection spectra indicated that NiO NPs enhance reflection intensity. In NiO NPs-PVDF//ZnO cells, the pumping threshold for fluorescence emission from DCM-doped CLCs decreased, while thermal-dependent quenching and time-dependent quenching was improved. When comparing the emission performance of DCM in the 8 wt% NiO NPs-PVDF//ZnO cell against those with PVDF//NiO cell, the former threshold pumping energy of DCM decreased to 0.317 μJ/pulse, the thermal-dependent quenching indicated that the emission of DCM maintained at 32.13% of its initial value, with a suppress of 5.11% in comparison to DCM in PVDF//ZnO cell. To further enhance DCM emission, photonic Au NRs were incorporated into the CLC-host. The Au NRs self-assembled into helical assemblies within the CLCs, and thermal stimulation was shown to modulate the photonic band gap of the Au NRs blending CLC-host, accompanied by changes in pitch and reflection. Moreover, the incorporation of Au NRs altered the near-field enhancement distribution across domains, promoting favorable dipole alignment of DCM and reducing pumping threshold. Additionally, emission characteristics such as thermal stability, quenching resistance, and temporal stability were improved. The threshold pumping energy of DCM in 1.0 wt% Au NRs blending CLC-host has been determined as 0.276 μJ/pulse, and when the host was heated near the clearing point of the LCs, the DCM emission maintained 41.48% of its initial intensity—a 9.35% suppression of thermal quenching compared to the pure CLC-host. After 60 minutes of continuous pumping, the emission intensity remained at 49.7%, corresponding to a similar time-dependent quenching relative to the reference.

These results demonstrate that integrating a functionalized PVDF alignment layer with a photonic CLC-host offers a robust and effective strategy for advancing the performance of LC-lasers, thereby facilitating their deployment in advanced optoelectronic applications. The resulting structural enhancements exemplified by a significant reduction in pumping threshold, improved operational stability, and greater integration potential, markedly broaden the scope of LC-laser applications beyond traditional uses in display technologies and optical communications. With their inherently tunable and coherent emission, LC-lasers are poised to drive transformative advancements in emerging fields such as holographic displays, and to support the convergence of solid-state lighting with high-speed optical wireless communication systems. Collectively, these developments are expected to propel LC-lasers from specialized laboratory tools toward becoming versatile and scalable platforms integral to next-generation photonic systems.

Electronic Supplementary Material: Supplementary material (which details the electro-optical performance of LCs in NPs-PVDF cells, the reflection spectra of CLCs in such cells, and the properties of Au NRs/CLC blends at various concentrations) is available in the online version of this article at https://doi.org/10.26599/NR.2026.94908811.

Data availability

All data needed to support the conclusions in the paper are presented in the manuscript and/or the Electronic Supplementary Material. Additional data related to this paper may be requested from the corresponding author upon request.

Acknowledgements

This work is granted by Natural Science Foundation of Shanghai (22ZR1401400) and National Natural Science Foundation of China (62241503).

Declaration of competing interest

All the contributing authors report no conflict of interests in this work.

Author contribution statement

Yang Liu: Conceptualization (lead), Funding acquisition (lead), Investigation (equal), Project administration (lead), Resources (lead), Supervision (lead), Visualization (lead), Writing - original draft (equal), Writing - review & editing (lead). Chunyang Dai: Investigation (equal), Methodology (lead), Writing - original draft (equal). Xiaohui Gong: Methodology (supporting). Hao Liu: Project administration (supporting), Funding acquisition (supporting). Yongfang Zhang: Project administration (supporting), Funding acquisition (supporting). Jianhua Shang: Project administration (supporting), Funding acquisition (supporting), Supervision (supporting). All the authors have approved the final manuscript.

Use of AI statement

None.

References

[1] Zhan, X.; Xu, F.-F.; Zhou, Z.; Yan, Y.; Yao, J.; Zhao, Y. S. 3D laser displays based on circularly polarized lasing from cholesteric liquid crystal arrays. *Adv. Mater.* **2021**, 33, 2104418.

[2] Gong, C.; Sun, F.; Yang, G.; Wang, C.; Huang, C.; Chen, Y.-C. Multifunctional laser imaging of cancer cell secretion with hybrid liquid crystal resonators. *Laser Photonics Rev.* **2022**, 16, 2100734.

[3] Cui, N.; Zhang, C.; Wang, H.; Fu, L.; Zhang, F.; Liu, Y.; Guan, B. 2.46 MHz ultranarrow line width vertical-cavity surface-emitting lasers with cholesteric liquid crystals coupled cavity. *ACS Photonics* **2025**, 12, 737–746.

[4] Dai, Y.; Shi, L.; Song, Y.; Zou, Y.; Fan, J.; Fu, X.; Ma, X. Electrical liquid crystal integration with VCSEL arrays for tunable orthogonal polarization laser. *Opt. Express* **2024**, 32, 40755–40766.

[5] Tsao, Y.-C.; Chen, H.-Y.; Chen, Y.-F. An electrically tunable dual-mode laser based on self-assembled soft photonic liquid crystals. *Adv.*

Funct. Mater. **2024**, 34, 2311510.

[6] Qu, G.; Zhang, X.; Lu, L.; Li, S.; Du, W.; Cao, Z.; Li, C.; Zhang, L.; Zhou, K.; Wu, S.; Ma, J.; Gao, J.; Yu, B.; Hu, Z. Efficient and Tunable Liquid Crystal Random Laser Based on Plasmonic-Enhanced FRET. *Laser Photonics Rev.* **2023**, 17, 2300106.

[7] Liu, J.; Chen, Y.; Jin, F.; Wang, J.; Ikeda, T.; Jiang, L. Single-, dual-, triple-, and quadruple-wavelength surface-emitting lasing in blue-phase liquid crystal. *Adv. Mater.* **2022**, 34, 2108330.

[8] Ortega, J.; Folcia, C. L.; Etxebarria, J. Liquid-crystal-based resonant cavities as a strategy to design low-threshold electrically-tunable lasers. *Liq. Cryst.* **2021**, 49, 427–435.

[9] Ahmad, A.; Dai, H.; Feng, S.; Li, M.; Mehvish, D.; Mohamed, Z.; Araina, S.; Chena, Z. Recent advances in lasing phenomena in cholesteric liquid crystals: materials, mechanisms and applications. *Phys. Chem. Chem. Phys.* **2025**, 27, 15293–15309.

[10] Jeong, M.-Y.; Choi, H.-J.; Nam, Y.; Kwak, K. Quickly formed continuously tuneable laser in the full visible spectrum using cholesteric liquid crystal cells based on the electrothermal effect. *Laser Photonics Rev.* **2024**, 18, 2301256.

[11] Inoue, Y.; Sasaki, S.; Moritake, H. High-quality tuning of cholesteric liquid crystal lasers based on polymer composite system. *J. Appl. Phys.* **2020**, 127, 083104.

[12] Xiang, J.; Varanytsia, A.; Minkowski, F.; Paterson, D. A.; Storey, J. M. D.; Imrie, C. T.; Lavrentovich, O. D.; Palffy-Muhoray, P. Electrically tunable laser based on oblique heliconical cholesteric liquid crystal. *Proc. Natl. Acad. Sci. U.S.A.* **2016**, 113, 12925–12928.

[13] Lin, J.-H.; Shih, W.-C.; Xie, Z.-H.; Tsay, S.-Y.; Huang, C.-C. Thermal control band-edge lasing toward near IR from dye-doped cholesteric liquid crystal: Relatively stable operation at high temperatures. *Opt. Laser Technol.* **2024**, 174, 110592.

[14] Lu, H.; Shi, J.; Wang, Q.; Xue, Y.; Yang, L.; Xu, M.; Zhu, J.; Qiu, L.; Ding, Y.; Zhang, J. Tunable multi-mode laser based on robust cholesteric liquid crystal microdroplet. *Opt. Lett.* **2021**, 46, 5067–5070.

[15] Lee, S. S.; Kim, J. B.; Kim, Y. H.; Kim, S.-H. Wavelength-tunable and shape-reconfigurable photonic capsule resonators containing cholesteric liquid crystals. *Sci. Adv.* **2018**, 4, eaat8276.

[16] Liu, Y.; Gan, H.; Zhang, Y.; Shang, J. Tunable and prolonged emission of DCM in an intrinsic chiral CNT blending cholesteric liquid crystal-host. *Opt. Lett.* **2025**, 50, 6105–6108.

[17] Chou, Y.-H.; Lin, J.-D. Prolonged laser emission via a polymeric chiral nematic liquid crystal cavity with a microfluidic gain medium. *Opt. Lett.* **2025**, 50, 3205–3208.

[18] Xie, S.; Gao, S.; Wang, L.; Li, Y.; Dang, J.; Zhang, X.; Zhang, M. Low-threshold lasing in cholesteric liquid crystals enabled by asymmetric defect layer positioning. *Appl. Phys. Lett.* **2025**, 127, 091103.

[19] Zhou, D.; Zhou, Z.; Li, X.; Yao, L.; Cao, W.; Liu, Y. High-sensitivity miniature fiber-optic temperature probe based on cholesteric liquid crystal laser emission. *Opt. Lett.* **2025**, 50, 2437–2440.

[20] Cao, W.; Muñoz, A.; Palffy-Muhoray, P.; Taheri, B. Lasing in a three-dimensional photonic crystal of the liquid crystal blue phase II. *Nat. Mater.* **2002**, 1, 111–113.

[21] Kim, K.; Hur, S.-T.; Kim, S.; Jo, S.-Y.; Lee, B. R.; Song, M. H.; Choi, S.-W. A well-aligned simple cubic blue phase for a liquid crystal laser. *J. Mater. Chem. C* **2015**, 3, 5383–5388.

[22] Khatun, N.; Sridurai, V.; Gupta, R. K.; Nath, S.; Kanakala, M. B.; Garain, S.; Achalkumar, A. S.; Yelamaggad, C. V.; Nair, G. G. Effect of photonic band gap on photoluminescence in a dye-doped blue phase liquid crystal. *J. Phys. Chem. B* **2021**, 125, 11582–11590.

[23] Xie, R.-C.; Tsay, S.-Y.; Wu, J.-J.; Kuo, C.-C.; Zhang, H.; Lin, J.-H. Manipulation of plasmonic random laser from dye-doped liquid crystals inside photonic crystal fiber by the electric field. *Opt. Laser Technol.* **2022**, 151, 108013.

[24] Cho, S.; Yoshida, H.; Ozaki, M. Emission direction-tunable liquid crystal laser. *Adv. Opt. Mater.* **2020**, 8, 2000375.

[25] Yokoyama, S.; Mashiko, S.; Kikuchi, H.; Uchida, K.; Nagamura, T. Laser emission from a polymer-stabilized liquid-crystalline blue phase. *Adv. Mater.* **2006**, 18, 48–51.

[26] Adamow, A.; Szukalski, A.; Sznitko, L. Electrically controlled white laser emission through liquid crystal/polymer multiphases. *Light Sci. Appl.* **2020**, 9, 19.

[27] Chen, Y.; Zheng, C.; Yang, W.; Li, J.; Jin, F.; Zhang, W.; Sun, W.; Wang, P.; Li, L.; Wang, J.; Jiang, L. Stretchable blue phase liquid crystal lasers with optical stability based on small-strain nonlinear 3D asymmetric deformation. *Adv. Mater.* **2025**, 37, 2416448.

[28] Chen, Y.; Zheng, C.; Yang, W.; Li, J.; Jin, F.; Shi, L.; Wang, J.; Jiang, L. Super-wide temperature lasers spanning from −180 to 240 °C based on fully-polymerized blue phase superstructures. *Adv. Mater.* **2024**, 36, 2308439.

[29] Liu, Y.; Wang, Y.; Wei, X.; Liu, H.; Zhang, Y. Enhanced laser emission by incorporating helically twisted silver nanoflakes within polymer-stabilized cholesteric liquid crystals. *ACS Photonics* **2024**, 11, 4873–4882.

[30] Wan, Y.; An, Y.; Deng, L. Plasmonic enhanced low-threshold random lasing from dye-doped nematic liquid crystals with TiN nanoparticles in capillary tubes. *Sci. Rep.* **2017**, 7, 16185.

[31] Liu, Y.; Sun, S.; Zhang, H.; Zhang, Y.; Shang, J. Photoconductive NiO/ZnO nanoparticles lightning the random laser emitted from a cholesteric liquid crystal host. *APL Photonics* **2025**, 10, 066103.

[32] Liu, Y.; Chen, J.; Wei, X. Tunable emission from spatially confined luminescent dye blending cholesteric liquid crystals within Au-nanocages. *Nano Res.* **2025**, 18, 880–893.

[33] Song, Y.; Fan, W.; Sun, J.; Huang, D.; Cheng, H.; Pan, H.; Wang, F. High laser damage threshold GaN-based liquid crystal devices for 2 μm band applications. *Infrared Phys. Technol.* **2025**, 146, 105768.

[34] Zhang, X.; Yang, Y.; Xue, P.; Valenzuela, C.; Chen, Y.; Yang, X.; Wang, L.; Feng, W. Three-Dimensional Electrochromic Soft Photonic Crystals Based on MXene-Integrated Blue Phase Liquid Crystals for Bioinspired Visible and Infrared Camouflage. *Angew. Chem. Int. Ed.* **2022**, 61, e202211030.

[35] Matsuhisa, Y.; Huang, Y.; Zhou, Y.; Wu, S.; Takao, Y.; Fujii, A.; Ozaki, M. Cholesteric liquid crystal laser in a dielectric mirror cavity upon band-edge excitation. *Opt. Express* **2007**, 15, 616–622.

[36] Chen, S.; Yu, H.; Zhang, W.; Shen, R.; Guo, W.; DeLuca, L. T.; Wang, H.; Ye, Y. Sponge-like Al/PVDF films with laser sensitivity and high combustion performance prepared by rapid phase inversion. *Chem. Eng. J.* **2020**, 396, 124962.

[37] Kim M.; Fan J. Piezoelectric Properties of Three Types of PVDF and ZnO Nanofibrous Composites. *Adv. Fiber Mater.* **2021**, 3, 160–171.

[38] Venkatesan H. M.; Arun A. P. Nickel-Oxide-Doped Polyvinylidene Fluoride Nanofiber-Based Flexible Triboelectric Nanogenerator for Energy Harvesting and Healthcare Monitoring Applications. *ACS Appl. Electron. Mater.* **2024**, 6, 1161–1173.

[39] Ma, Y.; Qin, Y.; Porter, M.; Spencer, J.; Du, Z.; Xiao, M.; Wang, B.; Wang, Y.; Jacobs, A. G.; Wang, H.; Tadjer, M.; Zhang, Y. Wide-Bandgap Nickel Oxide with Tunable Acceptor Concentration for Multidimensional Power Devices. *Adv. Electron. Mater.* **2025**, 11, 2300662.

Electronic Supplementary Material

Pulsed pumping on piezoelectric PVDF alignment layer suppresses emission consumption of DCM within cholesteric liquid crystal-host

Yang Liu, Chunyang Dai, Xiaohui Gong, Hao Liu, Yongfang Zhang, and Jianhua Shang

School of Information and Intelligent Science, Donghua University, 2999 North Renmin Road, Songjiang District, Shanghai 201620, China

Address correspondence to Yang Liu, liuyang@dhu.edu.cn; Jianhua Shang, jhshang@dhu.edu.cn

Supporting information to https://doi.org/10.26599/NR.2026.94908811

Table S1. Threshold voltage and response time of the NiO NPs-PVDF//ZnO cells under forward bias and reverse bias driving, respectively.

		V_{th} (V)	V_{th}/d (V/um)	t_r (ms)	t_f (ms)
Forward bias	PVDF//ZnO	1.371	0.274	4.143	16.816
	2 wt% NiO NPs-PVDF//ZnO	1.339	0.268	3.476	10.921
	4 wt% NiO NPs-PVDF//ZnO	1.302	0.260	2.987	9.377
	6 wt% NiO NPs-PVDF//ZnO	1.196	0.239	1.830	5.775
	8 wt% NiO NPs-PVDF//ZnO	0.972	0.194	1.596	5.227
Reverse bias	PVDF//ZnO	1.444	0.289	4.634	17.094
	2 wt% NiO NPs-PVDF//ZnO	1.401	0.280	6.286	25.976
	4 wt% NiO NPs-PVDF//ZnO	1.315	0.263	3.893	22.083
	6 wt% NiO NPs-PVDF//ZnO	1.215	0.243	3.440	11.372
	8 wt% NiO NPs-PVDF//ZnO	1.099	0.220	2.301	10.231

Table S2. Threshold voltage and response time of the ZnO NPs-PVDF//NiO cells under forward bias and reverse bias driving, respectively.

		V_{th} (V)	V_{th}/d (V/um)	t_r (ms)	t_f (ms)
Forward bias	PVDF//NiO	1.448	0.290	4.300	13.540
	2 wt% ZnO NPs-PVDF//NiO	1.399	0.280	3.543	13.718
	4 wt% ZnO NPs-PVDF//NiO	1.367	0.273	3.117	11.856
	6 wt% ZnO NPs-PVDF//NiO	1.326	0.265	2.189	10.392
	8 wt% ZnO NPs-PVDF//NiO	1.198	0.240	1.708	9.457
Reverse bias	PVDF//NiO	1.474	0.295	4.549	20.096
	2 wt% ZnO NPs-PVDF//NiO	1.455	0.291	3.770	17.719
	4 wt% ZnO NPs-PVDF//NiO	1.393	0.279	3.567	16.674
	6 wt% ZnO NPs-PVDF//NiO	1.308	0.262	2.947	13.859
	8 wt% ZnO NPs-PVDF//NiO	1.219	0.244	2.331	13.425

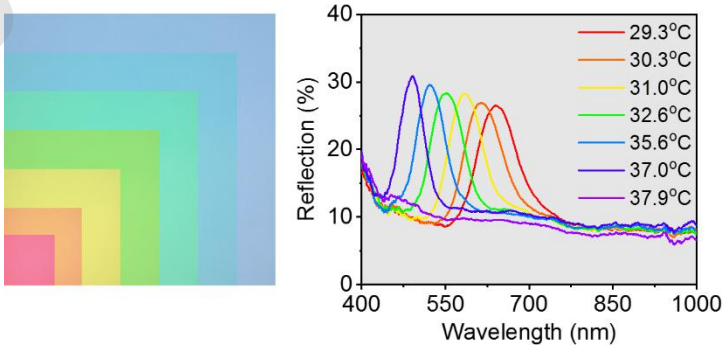

Figure S1. POM and reflection spectra of CLCs sandwiched in a PVDF//ZnO cell.

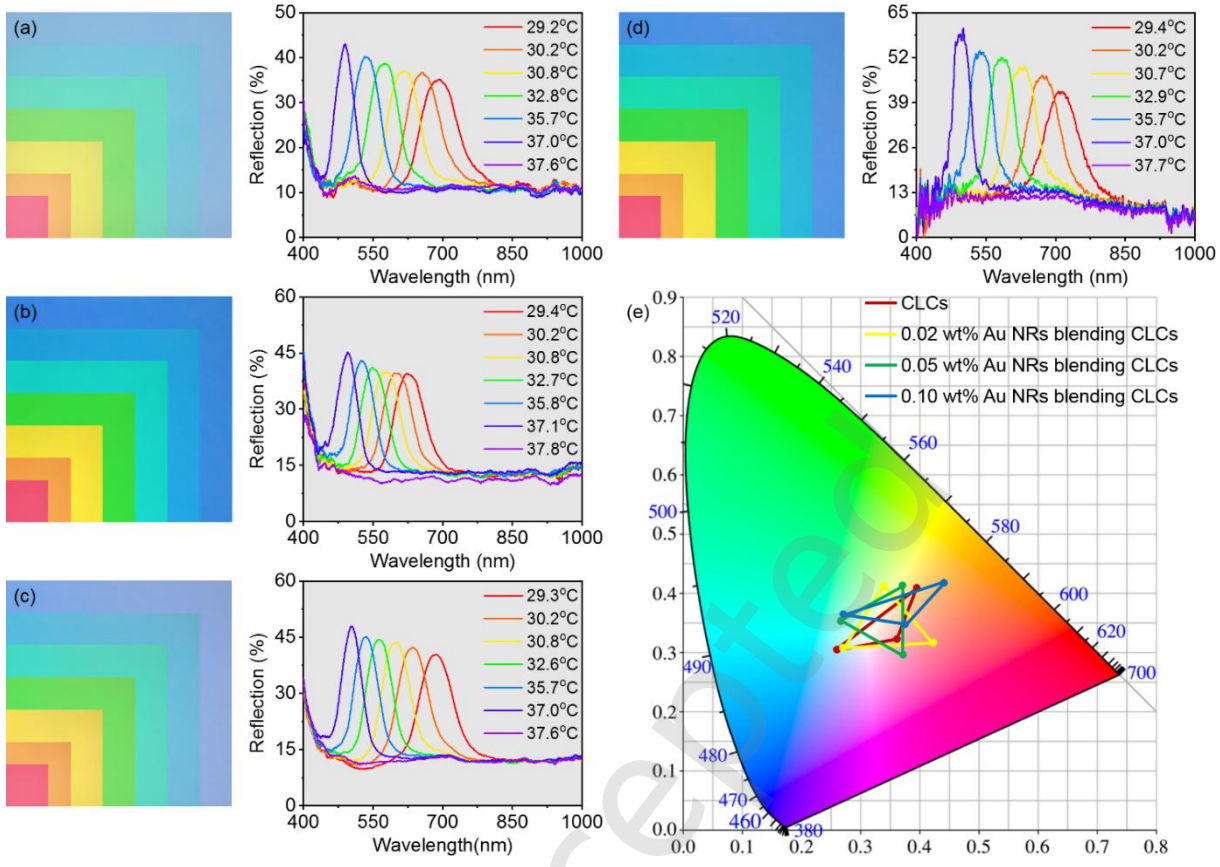

Figure S2. (a-d) are POM images and the corresponding dynamic reflectance spectra of Au NRs blending CLCs in 8 wt% NiO NPs-PVDF//ZnO cells under thermal stimuli at blending concentrations of 0.02 wt%, 0.05 wt% and 0.10 wt%, respectively, and (e) is the summary CIE diagram of the reflection.